



Title	Thermoelectric phase diagram of the SrTiO ₃ -LaTiO ₃ solid-solution system through a metal to Mott insulator transition
Author(s)	Zhang, Yuqiao; Sugo, Kenyu; Cho, Hai Jun; Ohta, Hiromichi
Citation	Journal of Applied Physics, 126(7), 075104 https://doi.org/10.1063/1.5100993
Issue Date	2019-08-21
Doc URL	http://hdl.handle.net/2115/79094
Rights	The following article appeared in Yuqiao Zhang, Kenyu Sugo, Hai Jun Cho, Hiromichi Ohta. Thermoelectric phase diagram of the SrTiO ₃ -LaTiO ₃ solid-solution system through a metal to Mott insulator transition, Journal of Applied Physics 126, 075104 (2019) and may be found at https://doi.org/10.1063/1.5100993 .
Type	article
File Information	1.5100993.pdf



[Instructions for use](#)

Thermoelectric phase diagram of the SrTiO₃-LaTiO₃ solid-solution system through a metal to Mott insulator transition

Cite as: J. Appl. Phys. **126**, 075104 (2019); <https://doi.org/10.1063/1.5100993>

Submitted: 23 April 2019 . Accepted: 20 July 2019 . Published Online: 15 August 2019

Yuqiao Zhang , Kenyu Sugo, Hai Jun Cho , and Hiromichi Ohta 

COLLECTIONS

Paper published as part of the special topic on [Advanced Thermoelectrics](#)

Note: This paper is part of the special topic on [Advanced Thermoelectrics](#).



View Online



Export Citation



CrossMark

ARTICLES YOU MAY BE INTERESTED IN

[Influence of pressure assisted sintering and reaction sintering on microstructure and thermoelectric properties of bi-doped and undoped calcium cobaltite](#)

Journal of Applied Physics **126**, 075102 (2019); <https://doi.org/10.1063/1.5107476>

[Mechanisms underpinning the ultrahigh piezoelectricity in Sm-doped 0.705Pb\(Mg_{1/3}Nb_{2/3}\)O₃-0.295PbTiO₃: Temperature-induced metastable local structure and field-induced polarization rotation](#)

Journal of Applied Physics **126**, 075101 (2019); <https://doi.org/10.1063/1.5089477>

[Experimental determination of the electro-acoustic properties of thin film AlScN using surface acoustic wave resonators](#)

Journal of Applied Physics **126**, 075106 (2019); <https://doi.org/10.1063/1.5094611>

Lock-in Amplifiers
Find out more today



Zurich Instruments



Thermoelectric phase diagram of the SrTiO₃-LaTiO₃ solid-solution system through a metal to Mott insulator transition

Cite as: J. Appl. Phys. 126, 075104 (2019); doi: 10.1063/1.5100993

Submitted: 23 April 2019 · Accepted: 20 July 2019 ·

Published Online: 15 August 2019



Yuqiao Zhang,^{1,a)} Kenyu Sugo,² Hai Jun Cho,^{1,2} and Hiromichi Ohta^{1,2,a)}

AFFILIATIONS

¹Research Institute for Electronic Science, Hokkaido University, N20W10, Kita, Sapporo 001-0020, Japan

²Graduate School of Information Science and Technology, Hokkaido University, N14W9, Kita, Sapporo 060-0814, Japan

Note: This paper is part of the special topic on Advanced Thermoelectrics.

a) Authors to whom correspondence should be addressed: eva_005@i26.com and hiromichi.ohta@es.hokudai.ac.jp

ABSTRACT

Systematic clarification of thermoelectric properties of a solid-solution system is essentially important, especially if the materials have different crystal and electronic structures. Here, we report the thermoelectric phase diagram of the full-range Sr_{1-x}La_xTiO₃ solid solutions composed of a band insulator SrTiO₃ (cubic perovskite) and a Mott insulator LaTiO₃ (distorted perovskite), which shows the room temperature thermoelectric power factor changing pattern with the La substitution (x) in the SrTiO₃ system. We measured the room temperature thermoelectric properties of Sr_{1-x}La_xTiO₃ ($0.01 \leq x \leq 1$) epitaxial films grown by the pulsed laser deposition and found that there are two thermoelectric phase boundaries at $x \sim 0.5$ and $x \sim 0.7$ in the Sr_{1-x}La_xTiO₃ system. The former is attributed to the lattice distortion from cubic to orthorhombic variation, whereas the latter is due to the electronic phase transition from metal to Mott insulator. The thermoelectric phase diagram obtained in our study will be fruitful for the future design of n-type thermoelectric materials based on the electron-doped SrTiO₃.

Published under license by AIP Publishing. <https://doi.org/10.1063/1.5100993>

I. INTRODUCTION

Thermoelectric technology, which can utilize the Seebeck effect to directly convert a temperature difference into electricity, is attracting increasing attention as an energy harvesting technique.^{1,2} The overall performance of the thermoelectric materials is generally characterized by the dimensionless figure of merit, $ZT = S^2 \cdot \sigma \cdot T \cdot \kappa^{-1}$, where Z is the figure of merit, S is the thermopower (\equiv Seebeck coefficient), σ is the electrical conductivity, and κ is the thermal conductivity. Although a number of high ZT metal chalcogenides, skutterudites, and half-Heusler materials, such as Bi₂Te₃ ($ZT \sim 1.86$ at 320 K),³ PbTe ($ZT \sim 2.2$ at 900 K),⁴ n-type SnSe ($ZT \sim 2.8$ at 773 K),⁵ Ba_{0.3}Yb_{0.3}Fe_{0.4}Co_{3.6}Sb₁₂ ($ZT \sim 1.35$ at 800 K),⁶ Ca_xCe_{0.35}Nd_{0.35}Fe_{4-y}Co_ySb₁₂ ($ZT \sim 1.1$ at 750 K),⁷ Ti_{0.5}Zr_{0.25}Hf_{0.25}NiSn ($ZT \sim 1.2$ at 830 K),⁸ and Nb_{0.6}Ti_{0.4}FeSb_{0.95}Sn_{0.05} ($ZT \sim 1$ at 973 K)⁹ have been reported, they are not ideal for converting wasted heat from automobiles, industries, and power plants because of their low thermal/chemical robustness and toxicity. For example, the melting point of Bi₂Te₃ is 585 °C, but the exhaust heat from an automobile is ~ 700 °C.

Thus, another class of thermoelectric materials with high chemical stability is required to utilize the waste heat from practical heat sources in daily life.¹⁰

In regard to these issues, several transition metal oxides (TMOs) including Na_xCoO₂,^{11,12} Ca₃Co₄O₉,^{13,14} and SrTiO₃¹⁵⁻¹⁷ are being widely considered as alternative materials for thermoelectric power generations because they exhibit relatively high ZT at high temperatures with good chemical/thermal stability.¹⁰ Among TMOs, electron-doped SrTiO₃ is considered to be one of the most promising TMOs as high temperature n-type thermoelectrics.^{18,19} In 2001, Okuda *et al.* observed comparable power factor ($PF = S^2 \cdot \sigma$) to the commercial Bi₂Te₃ in Sr_{1-x}La_xTiO₃ ($0 \leq x \leq 0.1$) single crystals at room temperature.¹⁵ Later, Ohta *et al.* reported the carrier transport properties of Nb- and La-doped SrTiO₃ single crystals and epitaxial films (carrier concentration, $n \sim 10^{21} \text{ cm}^{-3}$) at high temperatures (~ 1000 K) to clarify the intrinsic thermoelectric properties of these materials.^{16,17} In 2007, Ohta *et al.* also fabricated SrTi_{0.8}Nb_{0.2}O₃|SrTiO₃-based superlattices and observed very large S of the two-dimensional electron gas.²⁰⁻²³ However, while the

SrTiO₃-based materials exhibited adequate power factors comparable to conventional heavy-metal based thermoelectric materials, the overall ZT values were low (~ 0.1 at 300 K and ~ 0.3 at 1000 K) due to their high thermal conductivities.^{19,24}

The thermal conductivities of TMOs are difficult to reduce since the transition metal-oxygen bonds are usually strong and exhibit very high effective spring constants. Therefore, designing TMO-based thermoelectric modules greatly depends on improving their power factors. The electrical properties of TMOs come from the overlapping orbitals of the transition metal ions. For this reason, their electrical properties can be significantly modulated with atomic substitutions, and TMO solid solutions are very interesting in thermoelectric applications. In 2017, we systematically investigated the effect of changing the conduction band of SrTiO₃ from Ti^{3d} to Nb^{4d} and clarified the thermoelectric phase diagram for SrTi_{1-x}Nb_xO₃ solid solutions ($0.05 \leq x \leq 1$, hereafter SrTi_{1-x}Nb_xO₃ ss) using epitaxial films.²⁵ The fundamental thermoelectric properties of SrTi_{1-x}Nb_xO₃ ss found in this study was utilized in the fabrication of SrTi_{1-x}Nb_xO₃ ss|SrTiO₃ superlattices, which yielded PF two times higher ($5 \text{ mW m}^{-1} \text{ K}^{-2}$) than their bulk counterparts.²⁶ This phenomenon was attributed to the longer de Broglie wavelength of heavily Nb-substituted SrTi_{1-x}Nb_xO₃ ss and electron confinement effects in the superlattice, which was predicted by Hicks and Dresselhaus.²⁷⁻²⁹ This demonstrates that understanding TMO solid solutions can be the key to overcoming the limitations in oxide based thermoelectric modules.

Since the electrical properties of TMOs are drastically affected by electron-lattice coupling, examining SrTiO₃-LaTiO₃ solid solutions can provide insights into how thermoelectric properties of TMOs can be engineered.

La-doping to SrTiO₃ lattice is also commonly used to control the electrical conductivity of SrTiO₃, and SrTiO₃-LaTiO₃ is interesting SrTiO₃-based solid-solution system. Unlike the previous Ti \rightarrow Nb substitutions, the conduction band of the system is always comprised of Ti^{3d} orbitals during of Sr \rightarrow La substitutions. Compared to SrTiO₃, the atomic bonds in LaTiO₃ are highly distorted, which changes the electronic property from a band insulator to a Mott insulator. In fact, several research studies have been conducted on Sr_{1-x}La_xTiO₃^{15,30,31} and their superlattices,³² they are all limited by the solubility limit of La³⁺ ion into SrTiO₃ lattice ($x < \sim 0.1$),³³ and the thermoelectric properties of heavily La-doped SrTiO₃ are still lacking in the literature. Here, we focus on Sr_{1-x}La_xTiO₃ solid solutions (Sr_{1-x}La_xTiO₃ ss). We successfully varied x in Sr_{1-x}La_xTiO₃ ss epitaxial films from 0.01 to 1 by the pulsed laser deposition (PLD) and systematically clarified the thermoelectric phase diagram of Sr_{1-x}La_xTiO₃ ss. Despite the existence of two structural phase boundaries, only one electronic phase boundaries were revealed at $x \sim 0.7$, which originate from a local minimum in the carrier relaxation time and a transition from metal to Mott insulator, respectively. The thermoelectric phase diagram deduced in our study will be fruitful for the future design of n-type thermoelectric materials based on the electron-doped SrTiO₃.

II. EXPERIMENTAL

Approximately 100-nm-thick Sr_{1-x}La_xTiO₃ ($x = 0.01, 0.05, 0.1, 0.2, 0.3, 0.4, 0.5, 0.6, 0.7, 0.8, 0.9, \text{ and } 1.0$) epitaxial films were

fabricated by PLD using dense ceramic disks of SrTiO₃-LaTiO₃ mixtures. Insulating (001) LaAlO₃ (pseudocubic perovskite, $a = 3.79 \text{ \AA}$) were used as the substrate. The substrate temperature was kept at 950 °C, while the oxygen pressure was $\sim 5 \times 10^{-4} \text{ Pa}$. A laser fluence of $\sim 0.7 \text{ J cm}^{-2} \text{ pulse}^{-1}$ and a frequency of 5 Hz were used, yielding a growth rate of $\sim 6 \text{ pm pulse}^{-1}$. During the film growth, the reflection high energy electron diffraction (RHEED) pattern from the film surface was monitored to ensure the growth of high-quality epitaxial films. Details of the PLD growth system have been described elsewhere.^{17,34,35}

Crystallographic analyses of the resultant films were performed by high-resolution X-ray diffraction (XRD, Cu K α_1 , ATX-G, Rigaku Co.). Electrical conductivity (σ), carrier concentration (n), and Hall mobility (μ_{Hall}) were measured at room temperature by the conventional d.c. four-probe method, using an In-Ga alloy electrode with van der Pauw geometry. Thermopower (S) was measured at room temperature by creating a temperature difference (ΔT) of $\sim 4 \text{ K}$ across the film using two Peltier devices while monitoring the actual temperatures of each end of the Sr_{1-x}La_xTiO₃ films using two small thermocouples.^{36,37} The thermo-electromotive force (ΔV) and ΔT were measured simultaneously, and S -values were obtained from the slope of the ΔV - ΔT plots. In the electrical measurements, 3-5 samples were prepared at the same composition, which were used to obtain the average values and error bars.

III. RESULTS AND DISCUSSION

Figure 1 shows the schematic illustrations of (a) the crystal structures and (b) electronic energy band configurations of SrTiO₃ and LaTiO₃. SrTiO₃ (space group: $Pm\bar{3}m$, cubic perovskite structure, $a = 3.905 \text{ \AA}$) is a band insulator with a bandgap of 3.2 eV, in which the bottom of the conduction band is composed of triply degenerate, empty Ti 3d- t_{2g} orbitals, while the top of the valence band is composed of fully occupied O 2p orbitals.³⁸ On the other hand, LaTiO₃ (space group: $Pbnm$, orthorhombic structure, $a = 5.633 \text{ \AA}$, $b = 5.614 \text{ \AA}$, $c = 7.940 \text{ \AA}$) with one d electron per site is a typical Mott insulator due to the strong Coulomb interactions.^{39,40} As La³⁺ replaces Sr²⁺, the electrical properties of SrTiO₃ changes to a degenerate semiconductor with metallic behaviors. However, as La³⁺ substitution increases toward 100%, the conduction band in the SrTiO₃ phase will split into upper and bottom Hubbard bands with the Fermi level (E_F) located in between the two bands [Fig. 1(b)].

Sr²⁺ \rightarrow La³⁺ also induces structural changes. The orthorhombic $Pbnm$ structure (GdFeO₃ structure type) occurs in perovskite ABO_3 materials with Goldschmidt tolerance factor (t) less than 0.9, which is related to the ionic sizes.⁴¹ In 1992, Sunstrom *et al.* calculated the t values for all compositions of Sr_{1-x}La_xTiO₃ and found that orthorhombic $Pbnm$ structure is only stable at $x \geq 0.7$.⁴² Furthermore, Hays *et al.* observed a double phase transitions in Sr_{1-x}La_xTiO₃ ss ($0 < x \leq 1$), which are attributed to the cubic $Pm\bar{3}m$ to orthorhombic $Ibmm$ transition at $x \sim 0.3$ and orthorhombic $Ibmm$ to orthorhombic $Pbnm$ transition at $x \sim 0.7$.⁴³

To obtain the structural information from the Sr_{1-x}La_xTiO₃ ss, X-ray reciprocal space mappings (RSMs) around the 103 diffraction spot of LaAlO₃ were measured and summarized in Fig. 2(a). For comparison, the RSM results of SrTi_{1-x}Nb_xO₃ ss obtained from our previous study are also plotted.²⁵ Similar to SrTi_{1-x}Nb_xO₃ ss, all the

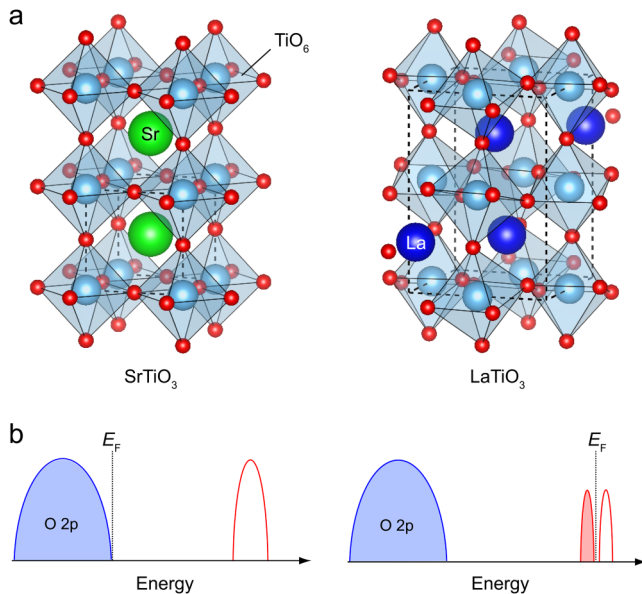


FIG. 1. Differences between SrTiO₃ and LaTiO₃. (a) Schematic crystal structure and (b) electronic band structure of SrTiO₃ and LaTiO₃. SrTiO₃ (space group: *Pm3m*, cubic perovskite structure, $a = 3.905 \text{ \AA}$) is a band insulator with a bandgap of 3.2 eV, in which the valence state of the Ti ions is 4+ (Ti 3d⁰). On the other hand, LaTiO₃ (space group: *Pbnm*, orthorhombic structure, $a = 5.635 \text{ \AA}$, $b = 5.618 \text{ \AA}$, $c = 7.917 \text{ \AA}$) is a Mott insulator with Fermi level (E_F) located at the Hubbard bandgap.

Sr_{1-x}La_xTiO₃ ss films are incoherently grown on LaAlO₃ substrates. However, in contrast to SrTi_{1-x}Nb_xO₃ ss, the diffraction spots of Sr_{1-x}La_xTiO₃ ss do not follow the cubic line ($q_z/q_x = -3$), which indicates that the Sr_{1-x}La_xTiO₃ ss lattices are distorted from the initial cubic structure. In particular, the deviation from the cubic relationship starts to become severe at $x > 0.5$, suggesting a crystal structure transition around $x = 0.6$. To further characterize the structural transition, we extracted the average distances between A-site atoms in perovskite ABO₃ (a) based on the formula $a = (2\pi/q_x \cdot 2\pi/q_x \cdot 6\pi/q_z)^{1/3}$. The results are plotted in Fig. 2(b), which also shows SrTi_{1-x}Nb_xO₃ ss for comparison.²⁵ In the case of SrTi_{1-x}Nb_xO₃ ss, all compositions of x follow the Vegard law (grey dash line) with an M-shaped tendency, which is attributed to the coexistence of isovalent and heterovalent substitutions. On the other hand, in the case of Sr_{1-x}La_xTiO₃, although the lattice parameter shows an increasing tendency due to the La substitution, an obvious deviation is observed from the Vegard law (red dash line). While the a values are certainly affected by compressive strains from LaAlO₃ substrates (3.79 Å), the deviations from the Vegard law observed from Sr_{1-x}La_xTiO₃ ss are much greater than those observed from SrTi_{1-x}Nb_xO₃ ss although they were all deposited on LaAlO₃ substrates. Therefore, the crystallographic changes in Sr_{1-x}La_xTiO₃ are strongly related to the A-site doping. A similar pattern from crystal structural transitions was also observed in La_{1-x}Ba_xTiO₃ system.⁴⁴ As described earlier, Sr_{1-x}La_xTiO₃ ss system has two phase transition points at $x \sim 0.3$ and $x \sim 0.7$. In Fig. 2(b), a change in the a value pattern can be identified at $x \sim 0.6$, which is likely attributed to the phase transition at $x \sim 0.7$. On the other hand, no noticeable changes in the a values were observed at $x \sim 0.3$.

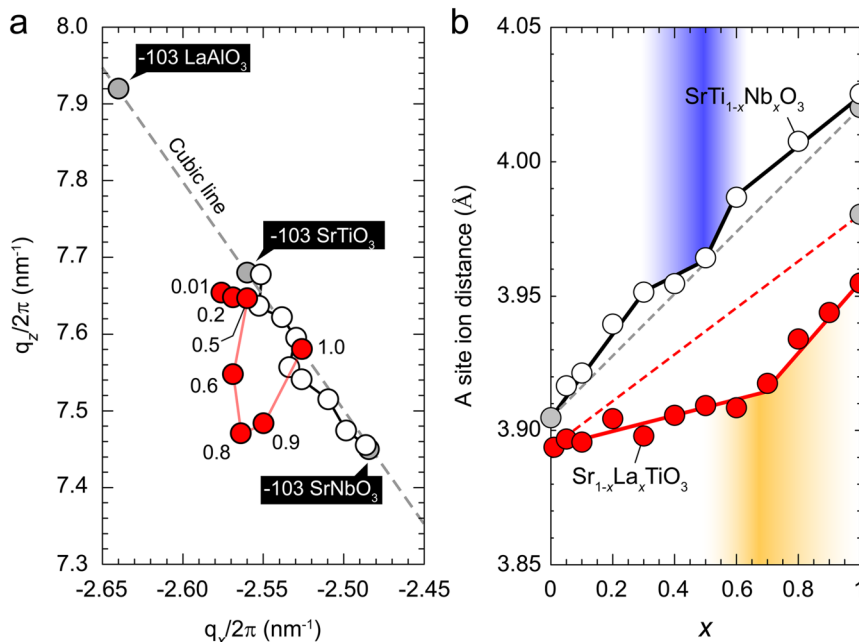


FIG. 2. Crystallographic characterization of the Sr_{1-x}La_xTiO₃ epitaxial films on a (001) LaAlO₃ single crystal substrate at room temperature. (a) Schematic illustrations of X-ray reciprocal space mappings around the (103) diffraction spot of the Sr_{1-x}La_xTiO₃ epitaxial films. The location of the LaAlO₃ diffraction spot ($q_x/2\pi, q_z/2\pi = (-2.64, 7.92)$), corresponds with the pseudocubic lattice parameter of LaAlO₃ ($a = 3.79 \text{ \AA}$). Red and white symbols indicate the peak positions of the Sr_{1-x}La_xTiO₃ and SrTi_{1-x}Nb_xO₃ epitaxial films, respectively. (b) Changing pattern of average A-site ionic distance of the Sr_{1-x}La_xTiO₃ (red symbols) and SrTi_{1-x}Nb_xO₃ (white symbols) epitaxial films $[(a^2 \cdot c)^{1/3}]$. All the films show a general increasing lattice constant. A V-shaped changing pattern was observed in Sr_{1-x}La_xTiO₃ films with a turning point located at $x \sim 0.7$, which indicates a crystal structure transitions from cubic *Pm3m* to orthorhombic *Pbnm*.

To clarify the electronic properties of the different phases in the $\text{Sr}_{1-x}\text{La}_x\text{TiO}_3$ ss system, we measured σ , n , and μ_{Hall} by Hall effect measurements and then compared the results with their $\text{SrTi}_{1-x}\text{Nb}_x\text{O}_3$ ss counterparts in Fig. 3.^{25,45} As shown in Fig. 3(a), σ of $\text{Sr}_{1-x}\text{La}_x\text{TiO}_3$ ss first increase with x when $x \leq 0.5$ and then decrease as x increases from 0.6 to 1. Similar to $\text{SrTi}_{1-x}\text{Nb}_x\text{O}_3$ ss, a jump in σ was observed between $0.5 < x < 0.6$, indicating an electronic phase boundary. σ usually depends on both n and μ_{Hall} . n increased with x , almost identical with the nominal value ($n = x$ in a unit cell) [Fig. 3(b)]. In addition, as shown in Fig. 3(c), μ_{Hall} keeps decreasing from $\sim 7.3 \text{ cm}^2 \text{ V}^{-1} \text{ s}^{-1}$ to $\sim 2.7 \text{ cm}^2 \text{ V}^{-1} \text{ s}^{-1}$ as x increases from 0.01 to 0.5. Okuda *et al.* reported $\sim 10 \text{ cm}^2 \text{ V}^{-1} \text{ s}^{-1}$ in slightly La-doped SrTiO_3 single crystals, which is higher than all μ_{Hall} values we obtained in the epitaxial films.¹⁵ This may be attributed to the lattice strain from the film/substrate mismatch, which is unavoidable in thin films in most cases. However, as x increases over 0.6, an obvious jump in μ_{Hall} can be observed, which agrees with Fig. 2(b). μ_{Hall} then keeps decreasing again to $\sim 0.5 \text{ cm}^2 \text{ V}^{-1} \text{ s}^{-1}$ at $x = 1$. Based on these results, similar to $\text{SrTi}_{1-x}\text{Nb}_x\text{O}_3$ ss, the electronic phase boundary between $0.5 < x < 0.6$ in $\text{Sr}_{1-x}\text{La}_x\text{TiO}_3$ ss is also dominated by the abrupt jump in μ_{Hall} .

The S of all $\text{Sr}_{1-x}\text{La}_x\text{TiO}_3$ ss films, which is related to the derivative of the density of states at the Fermi level, is shown in Fig. 3(d). $-S$ of $\text{Sr}_{1-x}\text{La}_x\text{TiO}_3$ ss exhibits a monotonic tendency, but a noticeable discontinuity is observed at $x = 0.7$, which is different from that

of the $\text{SrTi}_{1-x}\text{Nb}_x\text{O}_3$ ss films. In $\text{SrTi}_{1-x}\text{Nb}_x\text{O}_3$ ss, a conduction band transition from Ti 3d to Nb 4d at $x = 0.3$ was reported. However, after the transition, Nb 4d orbital shows lower carrier effective mass (m^*) than Ti 3d orbital, so $-S$ keeps decreasing within the full substitution range. In the case of $\text{Sr}_{1-x}\text{La}_x\text{TiO}_3$ ss, the conduction band is always comprised of the Ti 3d orbital. The hop in $-S$ reflects an increase in m^* , which is likely ascribed to the Mott transition. In order to directly confirm the increase in m^* , we calculated the density of states effective mass (m_{DOS}^*), on which the m^* is deduction is based $m^* = m_{\text{DOS}}^*/6$, using S and n according to Eqs. (1)–(3) below,⁴⁶

$$S = \frac{k_B}{e} \left(\frac{(r+2)F_{r+1}(\xi)}{(r+1)F_r(\xi)} - \xi \right), \quad (1)$$

where k_B , n , r , and F_r are the Boltzmann constant, chemical potential, scattering parameter of relaxation time, and Fermi integral, respectively. In the La-doped SrTiO_3 system around room temperature, the electron scattering is mainly affected by phonons.⁴⁷ Since the Debye temperatures of SrTiO_3 (694 K) and LaTiO_3 (500 K) are much greater than room temperature, the number of acoustic phonons is likely much higher than that of optical phonons, and the r value was assumed as 0.5, which represents electron-acoustic phonon scattering. Furthermore, the calculated carrier mean free path was much shorter than the average La^{3+} - La^{3+} ion distance, indicating that impurity

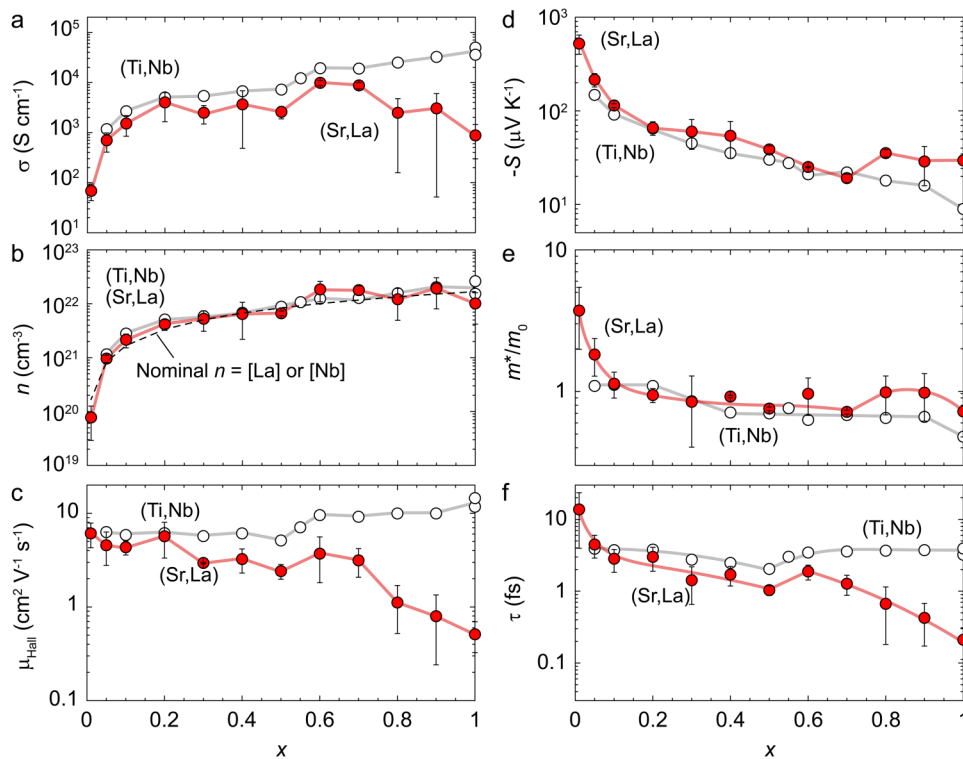


FIG. 3. Room temperature electron transport properties of $\text{Sr}_{1-x}\text{La}_x\text{TiO}_3$ epitaxial films: (a) electrical conductivity (σ), (b) carrier concentration (n), (c) Hall mobility (μ_{Hall}), (d) thermopower (S), (e) effective mass (m^*), (f) relaxation time (τ). Corresponding properties of $\text{SrTi}_{1-x}\text{Nb}_x\text{O}_3$ counterparts are also plotted for comparison (white symbols, from Refs. 25 and 45). The red and gray lines are drawn as a visual guide. Compared with single crystal data, our films show lower μ_{Hall} , which is likely to result from the higher defects.⁴⁸

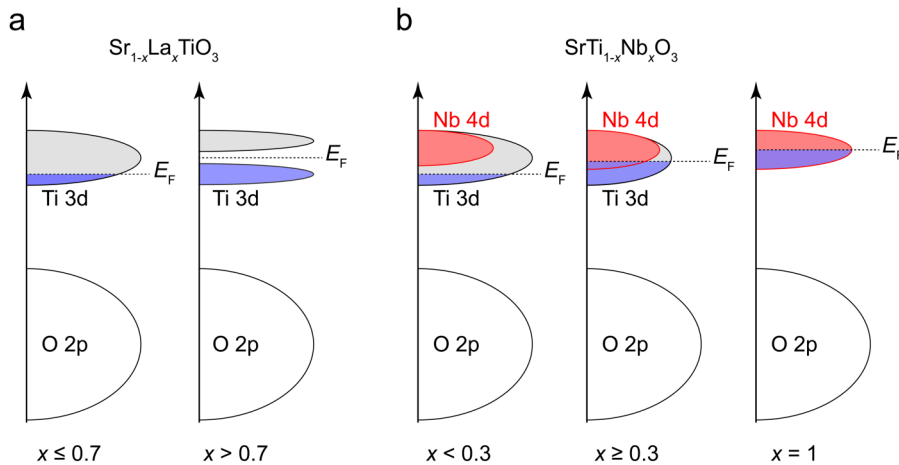


FIG. 4. Schematic illustrations of the band structure of $\text{Sr}_{1-x}\text{La}_x\text{TiO}_3$ epitaxial films (a) along with that of $\text{SrTi}_{1-x}\text{Nb}_x\text{O}_3$ counterparts (b) for comparison. In the $\text{Sr}_{1-x}\text{La}_x\text{TiO}_3$ case, a splitting of conduction band into upper Hubbard band (UHB) and lower Hubbard band (LHB) is prospected as $x > 0.7$, which furthermore results in the Mott insulating state in LaTiO_3 . For the $\text{SrTi}_{1-x}\text{Nb}_x\text{O}_3$ case, a conduction band transition from Ti 3d to Nb 4d was reported at $x \sim 0.3$.²⁵

scattering was not dominant in our system (Fig. S1 in the [supplementary material](#)). F_r is given by

$$F_r(\xi) = \int_0^{\infty} \frac{x^r}{1 + e^{x-\xi}} dx \quad (2)$$

and n is given by

$$n = 4\pi \left(\frac{2m_{\text{DOS}}^* k_B T}{h^2} \right)^{\frac{3}{2}} F_{\frac{3}{2}}(\xi), \quad (3)$$

where h and T are the Planck constant and absolute temperature, respectively. As shown in Fig. 3(e), the m^* monotonically decreases until $x = 0.7$. Between $0.7 < x < 0.8$, m^* shows an abrupt jump from $\sim 0.7 m_0$ to $\sim 1 m_0$ ($m_0 =$ rest mass of an electron). We believe this phenomenon is related to the Mott transition, where the conduction band starts to split into upper and bottom Hubbard bands. Our results are also very constant with other reports on either La- or Nb-doped SrTiO_3 systems, which shows the validity of our calculation process.^{48–51} The n-type conduction observed from the pure LaTiO_3 film ($x = 1$) may be attributed to an incomplete opening of Hubbard band.⁴³ The relaxation time (τ) extracted from μ_{Hall} and m^* values ($= e \cdot \tau \cdot m^*^{-1}$) are plotted in Fig. 3(f). For $0.01 \leq x \leq 0.5$, τ gradually decreases with x , reaching a local minimum of ~ 1.03 fs at $x = 0.5$. Afterward, τ slightly jumps and returns to a gradually decreasing tendency. The local minimum in τ at $x = 0.5$ suggests a very high electron scattering cross sections. As shown in Fig. 2(a), a severe lattice distortion in the $\text{Sr}_{1-x}\text{La}_x\text{TiO}_3$ ss films starts at $x \sim 0.5$, which will drastically increase the electron scattering. A similar phenomenon was also observed in $\text{SrTi}_{1-x}\text{Nb}_x\text{O}_3$ ss and Ca/Ba substituted $\text{SrTi}_{0.8}\text{Nb}_{0.2}\text{O}_3$ epitaxial films.^{25,34} Furthermore, during the orthorhombic $Pbnm$ transition, the bond angle of Ti–O–Ti deviates from 180° , reducing the effective d -electron hopping interaction, especially since the d -electron transfer was reported to be dominated by the supertransfer interaction via the O 2p states rather than the direct d – d hopping.⁵²

Based on the electrical properties, we further proposed a schematic illustration of electronic band structure evolution for $\text{Sr}_{1-x}\text{La}_x\text{TiO}_3$ ss [Fig. 4(a)] along with that of their $\text{SrTi}_{1-x}\text{Nb}_x\text{O}_3$ ss [Fig. 4(b)]. According to the changing pattern of m^* , the Mott transition seems to exist between $0.7 < x < 0.8$, where the Ti^{3d} orbital splits into an upper Hubbard band (UHB) and a lower Hubbard band (LHB). Theoretically, LaTiO_3 is a Mott insulator with E_F located between UHB and LHB or shows slight p-type conduction. However, in our experiment, $\text{Sr}_{1-x}\text{La}_x\text{TiO}_3$ at $x = 1$ exhibits a metallic behavior (ρ – T curve shown in Fig. S2 in the [supplementary material](#)) with an n-type conduction. This probably results from an incomplete opening of the Hubbard gap caused by the lattice deformation induced by the LaAlO_3 substrate.^{43,53} In comparison, the thermoelectric properties of $\text{SrTi}_{1-x}\text{Nb}_x\text{O}_3$ ss was

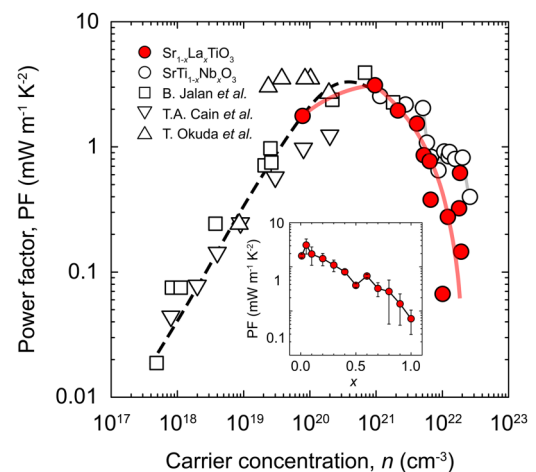


FIG. 5. Room temperature thermoelectric phase diagram for the $\text{Sr}_{1-x}\text{La}_x\text{TiO}_3$ solid-solution system. The thermoelectric power factor ($\text{PF} = S^2 \cdot \sigma$) of the $\text{Sr}_{1-x}\text{La}_x\text{TiO}_3$ solid-solution system is plotted, alongside the previously reported values.^{25,30,48,54} The x dependence of PF is shown in the inset.

dominated by the changes in the conduction band orbital. A conduction band transition from Ti 3d to Nb 4d was found at $x \sim 0.3$.²⁵ For SrNbO₃, with the d¹ configuration, it shows intrinsic high conductivity as a Fermi liquid.⁴⁵

Finally, we calculated the power factor ($PF = S^2 \cdot \sigma$) of Sr_{1-x}La_xTiO₃ ss and plotted with previously reported values from other reported films and bulk single crystals (Fig. 5).^{25,30,48,54} Similar with previous reports, Sr_{1-x}La_xTiO₃ ss first shows an increasing and then decreasing tendency as a function of n , reaching a peak value of $\sim 4.1 \text{ mW m}^{-1} \text{ K}^{-2}$ at $x = 0.05$ ($n \sim 10^{21} \text{ cm}^{-3}$). Our slightly La-substituted SrTiO₃ exhibits both high m^* and high μ_{Hall} , which realizes high S and σ values. With increasing x , m^* and μ_{Hall} decrease simultaneously, leading to a sharp decrease in PF. For heavily La-substituted samples, due to the Mott transition, electron transport deteriorates significantly. Despite of the similar n values, they show much lower PF than their heavily Nb-substituted counterparts. As shown in Fig. 5, if $x > 0.05$, PF keeps decreasing with x . At $x = 0.5$, we can see a small local minimum in PF, which should be originating from the electron transport property reduction. After the Mott transition ($x > 0.7$), there is no obvious PF enhancement due to the increase in m^* , which is not enough to compensate the deteriorating electron transport properties. Based on this thermoelectric phase diagram, it could be concluded that using slight electron doping would favor the optimization of thermoelectric performance for SrTiO₃-based thermoelectric materials.

IV. SUMMARY

In summary, we have clarified the thermoelectric phase diagram for the Sr_{1-x}La_xTiO₃ ss through the characterization of epitaxial films prepared by the PLD method. As we varied x , we observed lattice distortions from crystal structure transitions from a cubic structure to an orthorhombic structure, which results in a drastic increase in electron scattering. An electronic phase boundary was revealed by a local minimum in Hall mobility at $x \sim 0.5$, which is dominated by electron-lattice coupling and electron relaxation time reduction. Furthermore, a Mott transition was confirmed by a sudden hop in carrier effective mass observed between $0.7 < x < 0.8$. The slightly La-substituted region shows a similar tendency in PF with previous reports. However, due to the increasing carrier scattering and Mott insulating transition, the electron transport for the heavily La-substituted region deteriorates significantly, which results in a sharp decrease in PF. Even though thin film thermoelectric is not ideal from a real application, some intrinsic findings obtained in our research will still be fruitful for engineering the transport properties of SrTiO₃-based thermoelectric materials.

SUPPLEMENTARY MATERIAL

The supplementary material shows the room temperature carrier mean free path of Sr_{1-x}La_xTiO₃ epitaxial films and the temperature dependent resistivity of LaTiO₃ film which indicates a metallic behavior.

ACKNOWLEDGMENTS

Y.Z. was supported by Grants-in-Aid for JSPS International Research Fellow (19F19049). H.O. was supported by Grants-in-Aid for Scientific Research A (No. 17H01314) and Innovative Areas (19H05791) from the JSPS, the Asahi Glass Foundation, and the Mitsubishi Foundation. H.J.C. was supported by the Nippon Sheet Glass Foundation for Materials Science and Engineering. A part of this work was supported by the Dynamic Alliance for Open Innovation Bridging Human, Environment and Materials as well as the Network Joint Research Center for Materials and Devices.

REFERENCES

- 1 D. M. Rowe, *CRC Handbook of Thermoelectrics* (CRC Press, 1995).
- 2 G. J. Snyder and E. S. Toberer, *Nat. Mater.* **7**, 105 (2008).
- 3 S. Il. Kim, K. H. Lee, H. A. Mun, H. S. Kim, S. W. Hwang, J. W. Roh, D. J. Yang, W. H. Shin, X. S. Li, Y. H. Lee, G. J. Snyder, and S. W. Kim, *Science* **348**, 109 (2015).
- 4 K. Biswas, J. Q. He, I. D. Blum, C. I. Wu, T. P. Hogan, D. N. Seidman, V. P. Dravid, and M. G. Kanatzidis, *Nature* **489**, 414 (2012).
- 5 C. Chang, M. H. Wu, D. S. He, Y. L. Pei, C. F. Wu, X. F. Wu, H. L. Yu, F. Y. Zhu, K. D. Wang, Y. Chen, L. Huang, J. F. Li, J. Q. He, and L. D. Zhao, *Science* **360**, 778 (2018).
- 6 S. Ballikaya and C. Uher, *J. Alloys Compd.* **585**, 168 (2014).
- 7 T. Dahal, Q. Jie, W. S. Liu, K. Dahal, C. F. Guo, Y. C. Lan, and Z. F. Ren, *J. Alloys Compd.* **623**, 104 (2015).
- 8 M. Schwall and B. Balke, *Phys. Chem. Chem. Phys.* **15**, 1868 (2013).
- 9 G. Joshi, R. He, M. Engber, G. Samsonidze, T. Pantha, E. Dahal, K. Dahal, J. Yang, Y. C. Lan, B. Kozinsky, and Z. F. Ren, *Energy Environ. Sci.* **7**, 4070 (2014).
- 10 K. Koumoto, Y. F. Wang, R. Z. Zhang, A. Kosuga, and R. Funahashi, *Annu. Rev. Mater. Res.* **40**, 363 (2010).
- 11 I. Terasaki, Y. Sasago, and K. Uchinokura, *Phys. Rev. B* **56**, 12685 (1997).
- 12 M. Lee, L. Viciu, L. Li, Y. Y. Wang, M. L. Foo, S. Watauchi, R. A. Pascal, R. J. Cava, and N. P. Ong, *Nat. Mater.* **5**, 537 (2006).
- 13 S. W. Li, R. Funahashi, I. Matsubara, K. Ueno, and H. Yamada, *J. Mater. Chem.* **9**, 1659 (1999).
- 14 A. Masset, C. Michel, A. Maignan, M. Hervieu, O. Toulemonde, F. Studer, B. Raveau, and J. Hejtmanek, *Phys. Rev. B* **62**, 166 (2000).
- 15 T. Okuda, K. Nakanishi, S. Miyasaka, and Y. Tokura, *Phys. Rev. B* **63**, 113104 (2001).
- 16 S. Ohta, T. Nomura, H. Ohta, and K. Koumoto, *J. Appl. Phys.* **97**, 034106 (2005).
- 17 S. Ohta, T. Nomura, H. Ohta, M. Hirano, H. Hosono, and K. Koumoto, *Appl. Phys. Lett.* **87**, 092108 (2005).
- 18 H. Ohta, *Mater. Today* **10**, 44 (2007).
- 19 H. Ohta, K. Sugiura, and K. Koumoto, *Inorg. Chem.* **47**, 8429 (2008).
- 20 H. Ohta, S. Kim, Y. Mune, T. Mizoguchi, K. Nomura, S. Ohta, T. Nomura, Y. Nakanishi, Y. Ikuhara, M. Hirano, H. Hosono, and K. Koumoto, *Nat. Mater.* **6**, 129 (2007).
- 21 Y. Mune, H. Ohta, K. Koumoto, T. Mizoguchi, and Y. Ikuhara, *Appl. Phys. Lett.* **91**, 192105 (2007).
- 22 K. H. Lee, Y. Mune, H. Ohta, and K. Koumoto, *Appl. Phys. Express* **1**, 015007 (2008).
- 23 W. S. Choi, H. Ohta, S. J. Moon, Y. S. Lee, and T. W. Noh, *Phys. Rev. B* **82**, 024301 (2010).
- 24 J. W. Fergus, *J. Eur. Ceram. Soc.* **32**, 525 (2012).
- 25 Y. Q. Zhang, B. Feng, H. Hayashi, T. Tohei, I. Tanaka, Y. Ikuhara, and H. Ohta, *J. Appl. Phys.* **121**, 185102 (2017).

- ²⁶Y. Q. Zhang, B. Feng, H. Hayashi, C. P. Chang, Y. M. Sheu, I. Tanaka, Y. Ikuhara, and H. Ohta, *Nat. Commun.* **9**, 2224 (2018).
- ²⁷L. D. Hicks and M. S. Dresselhaus, *Phys. Rev. B* **47**, 12727 (1993).
- ²⁸L. D. Hicks, T. C. Harman, X. Sun, and M. S. Dresselhaus, *Phys. Rev. B* **53**, 10493 (1996).
- ²⁹N. T. Hung, E. H. Hasdeo, A. R. T. Nugraha, M. S. Dresselhaus, and R. Saito, *Phys. Rev. Lett.* **117**, 036602 (2016).
- ³⁰B. Jalan and S. Stemmer, *Appl. Phys. Lett.* **97**, 042106 (2010).
- ³¹W. S. Choi, H. K. Yoo, and H. Ohta, *Adv. Funct. Mater.* **25**, 799 (2015).
- ³²W. S. Choi, H. Ohta, and H. N. Lee, *Adv. Mater.* **26**, 6701 (2014).
- ³³B. R. Sudireddy and K. Agersted, *Fuel Cells* **14**, 961 (2014).
- ³⁴M. Yamamoto, H. Ohta, and K. Koumoto, *Appl. Phys. Lett.* **90**, 072101 (2007).
- ³⁵Y. Mune, H. Ohta, K. Koumoto, T. Mizoguchi, and Y. Ikuhara, *Appl. Phys. Lett.* **91**, 192105 (2007).
- ³⁶H. Ohta, Y. Sato, T. Kato, S. Kim, K. Nomura, Y. Ikuhara, and H. Hosono, *Nat. Commun.* **1**, 118 (2010).
- ³⁷H. Ohta, T. Mizuno, S. J. Zheng, T. Kato, Y. Ikuhara, K. Abe, H. Kumomi, K. Nomura, and H. Hosono, *Adv. Mater.* **24**, 740 (2012).
- ³⁸L. F. Mattheiss, *Phys. Rev. B* **6**, 4718 (1972).
- ³⁹M. Eitel and J. E. Greedan, *J. Less-Common Met.* **116**, 95 (1986).
- ⁴⁰M. Imada, A. Fujimori, and Y. Tokura, *Rev. Mod. Phys.* **70**, 1039 (1998).
- ⁴¹M. Higuchi, K. Aizawa, K. Yamaya, and K. Kodaira, *J. Solid State Chem.* **92**, 573 (1991).
- ⁴²J. Sunstrom, S. Kauzlarich, and P. Klavins, *Chem. Mater.* **4**, 346 (1992).
- ⁴³C. C. Hays, J. S. Zhou, J. T. Markert, and J. B. Goodenough, *Phys. Rev. B* **60**, 10367 (1999).
- ⁴⁴V. Fritsch, J. Hemberger, M. Brando, A. Engelmayer, S. Horn, M. Klemm, G. Knebel, F. Lichtenberg, P. Mandal, F. Mayr, M. Nicklas, and A. Loidl, *Phys. Rev. B* **64**, 045113 (2001).
- ⁴⁵D. Oka, Y. Hirose, S. Nakao, T. Fukumura, and T. Hasegawa, *Phys. Rev. B* **92**, 205102 (2015).
- ⁴⁶C. B. Vining, *J. Appl. Phys.* **69**, 331 (1991).
- ⁴⁷A. Verma, A. P. Kajdos, T. A. Cain, S. Stemmer, and D. Jena, *Phys. Rev. Lett.* **112**, 216601 (2014).
- ⁴⁸T. Okuda, K. Nakanishi, S. Miyasaka, and Y. Tokura, *Phys. Rev. B* **63**, 113104 (2001).
- ⁴⁹H. P. R. Frederikse, W. R. Thurber, and W. R. Hosler, *Phys. Rev.* **134**, A442 (1964).
- ⁵⁰M. Ahrens, R. Merkle, B. Rahmati, and J. Maier, *Phys. B Condens. Matter* **393**, 239 (2007).
- ⁵¹W. Gong, H. Yun, Y. Ning, J. Greedan, W. Datars, and C. Stager, *J. Solid State Chem.* **90**, 320 (1991).
- ⁵²W. A. Harrison, *Electronic Structure and the Properties of Solids: The Physics of the Chemical Bond* (Courier Corporation, 2012).
- ⁵³F. J. Wong, S. H. Baek, R. V. Chopdekar, V. V. Mehta, H. W. Jang, C. B. Eom, and Y. Suzuki, *Phys. Rev. B* **81**, 161101 (2010).
- ⁵⁴T. A. Cain, A. P. Kajdos, and S. Stemmer, *Appl. Phys. Lett.* **102**, 182101 (2013).